ORIGINAL PAPER

Evolution of mechanical behaviours of an expansive soil during drying-wetting, freeze–thaw, and drying-wetting-freeze–thaw cycles

Gui-tao Zhao[1] · Zhong Han[1,2] · Wei-lie Zou[1,2] · Xie-qun Wang[3]

Abstract

This paper investigates the volumetric, microstructural, and shear behaviours of an expansive soil during multiple drying-wetting (DW), freeze–thaw (FT), and drying-wetting-freeze–thaw (DWFT) cycles. Specimens compacted at natural moisture content and dry density were subjected to 1, 4, 6, and 10 DW, FT, or DWFT cycles. Volumetric changes were recorded during the treatments and mercury intrusion porosimetry, and scanning electron microscope tests were conducted to observe the soil's microstructure before and after treatments. As compacted specimens and specimens after different numbers of DW, FT, and DWFT cycles were saturated and sheared under consolidated undrained condition to determine their undrained elastic modulus (E_u), shear strength (q_u), total cohesion (c), and friction angle (ϕ). Experimental results show that DW, FT, and DWFT cycles mainly influence the soil's macropores with diameters between 5 and 250 μm. Macropores collapse during DW cycles, which lead to collapse in the soil's global volume. Cracks develop during FT cycles and result in slight swelling in the soil's volume. These two effects offset during DWFT cycles and cause an intermediate volumetric behaviour. The E_u, q_u, c, and ϕ decline during DW, FT, and DWFT cycles, and the reduction was most significant during DWFT cycles. They reach an equilibrium after approximately 6 cycles of treatment. A simple normalized model was developed to describe the stress–strain curves considering the influence of DW, FT, and DWFT cycles. Good agreements were achieved between the model predictions and measurements for all stress–strain curves obtained in this study.

Keywords Expansive soil · Microstructure · Drying-wetting · Freeze–thaw · Shear strength

Introduction

Expansive soils are widely found in many countries such as China, India, Canada, Israel, and Australia (Jones and Holtz 1973; Alonso et al. 1987). They are typically distributed close to the ground surface where they are exposed to various climate events such as evaporation, infiltration, and plant transpiration. Expansive soils are sensitive to moisture content variation, during which their bulk volume and microstructure change significantly. This results in complex evolution in their engineering properties such as permeability, shear strength, modulus, and volumetric behaviours (Tripathy et al. 2002; Vilar and Rodrigues 2011; Lu and Godt 2012; Ajdari et al. 2013; Zha et al. 2013; Zhang et al. 2015; Massat et al. 2016; Zou et al. 2018).

In seasonally frozen regions, in addition to the moisture fluctuation, expansive soils are also subjected to freezing and thawing processes in winter and spring. These environmental effects constitute periodical drying-wetting (DW) cycles, freeze–thaw (FT) cycles, and more realistically, combined drying-wetting-freeze–thaw (DWFT) cycles that act on surficial expansive soils. The thermal and moisture exchange associated with DW, FT, and DWFT cycles cause remarkable alterations in the bonding and arrangement of soil particles (Edwin and Anthony 1979; Xue et al. 2014; Liu et al. 2016), which lead to the deterioration in the engineering properties of expansive soils (Aubert and Gasc-Barbier 2012; Aldaood et al. 2014; Cui et al. 2014; Liu et al. 2016; Hu et al. 2019;

✉ Wei-lie Zou
zwilliam@whu.edu.cn

1   School of Civil Engineering, Wuhan University, Wuhan, Hubei, China

2   Key Laboratory of Hydraulic Rock Mechanics of Ministry of Education, Wuhan University, Wuhan, Hubei, China

3   School of Civil Engineering and Architecture, Wuhan University of Technology, Wuhan, Hubei, China

Qu et al. 2020; Zhou et al. 2020). This poses challenges to the design of geotechnical structures in expansive soils in seasonally frozen regions.

Over the past few decades, the effects of DW cycles and FT cycles on various soils have been investigated (Alonso et al. 2005; Nowamooz and Masrouri 2008; Tripathy et al. 2009; Tang et al. 2016; Zhao et al. 2019; Othman and Benson 1993; Kraus et al. 1997; Hewitt and Daniel 1997; Yuen et al. 1998; Hohmann-Porebska 2002; Luo et al. 2018; Ye and Li 2019; Dalla et al. 2019). Generally, it was found that both DW and FT cycles introduce cracks to the soils' structure. Cracks induced by DW cycles are mainly associated with the non-uniform development of the volumetric strain (Pires et al. 2008; Seiphoori et al. 2014; Monroy et al. 2010; Lin and Cerato 2014; Burton et al. 2015), while cracks induced by FT cycles are mainly the results of the internal pressure associated with the growth of ice lenses (Tian et al. 2019; Tang and Yan 2015).

DW- or FT-induced cracks weaken the integrity of soils' structure and create large and unstable pore spaces (Pires et al. 2008; Seiphoori et al. 2014; Graham and Au 1985; Zhang et al. 2016) that lead to (i) an increase in hydraulic conductivity (Albrecht and Benson 2001; Malusis et al. 2011; Edwin and Anthony 1979; Konrad and Samson 2000), (ii) remarkable changes in the bulk volume (Al-Homoud et al. 1995; Peng et al. 2007; Liu et al. 2016; Kalkan 2011; Wang et al. 2017; Luo et al. 2018), and (iii) degradation in the stiffness and strength properties (Wang et al. 2015; Tang et al. 2018; Xu et al. 2018; Lu et al. 2019). However, the combined effects of DW and FT cycles (i.e. DWFT cycles)

on the microstructure and mechanical behaviours of soils are less reported, especially for expansive soils.

This paper investigates the influence of DW, FT, and DWFT cycles on the mechanical behaviours and microstructure of a compacted expansive soil collected from Northeastern China. The investigated mechanical behaviours include elastic modulus and shear strength (i.e. cohesion and internal friction angle) that were obtained from consolidated undrained triaxial tests. Microstructural observations were performed through mercury intrusion porosimetry (MIP) and scanning electron microscope (SEM) tests to reveal the evolution of the soil structure. A constitutive model is proposed to describe the stress–strain relationships of the tested expansive soil considering the influence of DW, FT, and DWFT cycles.

Experimental investigations

Material

The expansive soil investigated in this study was collected from a failed canal slope in the north of Qiqihar, Heilongjiang Province, China, which is a seasonally frozen region (see Fig. 1). The climate type of Qiqihar belongs to the temperate continental monsoon climate which is featured by hot and rainy summer and cold and dry winter. The average temperature ranges from 23.1 °C in summer to −18.6 °C in winter and the average precipitation ranges from 103.0 to

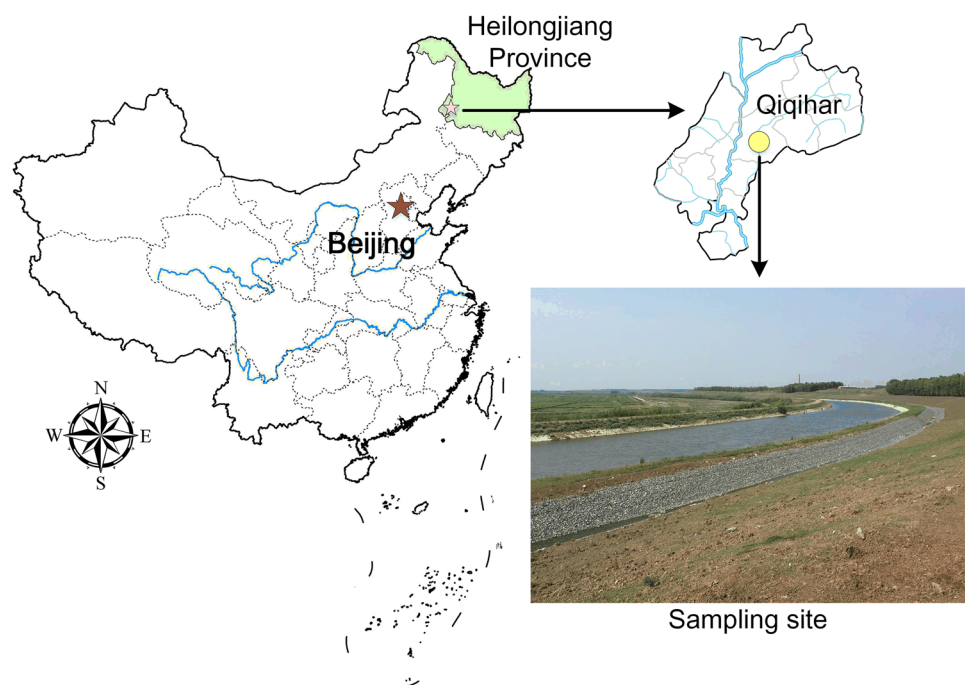**Fig. 1** Location of the tested expansive soil

Fig. 2 **a** Representative failed canal slope and the **b** crushing failure of concrete slabs on the canal bed

3.2 mm. The average frost depth and active zone depth in Qiqihar are approximately 2 m and 3 m, respectively.

The canal (i.e. sampling site) was designed for water diversion from Nen River, mainly to meet the water demands of the petrochemical industry and agricultural irrigation in the vicinity. The average slope angle was between 12.2 and 19.9°. The local geology comprises weak and medium expansive soils and locally dispersive soils. At the end of 2011, more than a dozen large or small landslides were found on the left-side slope of the canal. The total volume of the landslides was 32,925 m^3. A representative failed slope is shown in Fig. 2a. Due to the large-scale landslides, the concrete slabs on the canal bed were jacked up and the total damaged concrete is 717.6 m^3 (see Fig. 2b).

Field investigations and laboratory tests were conducted to investigate the causes of the slope failure. It was revealed that after excavation, the canal slope was directly exposed to the atmosphere with no protection. Besides, no slope drainage system was designed during the canal construction. Thus, cracks gradually develop on the slope surface due to the natural weathering effects (including cyclic drying-wetting-freeze–thaw effects), resulting in the acceleration of the infiltration of snowmelt and rainwater and the evaporation of soil moisture. During the weathering, the expansive soils experienced cyclic swelling and shrinkage, which facilitates the development of cracks. Such damages led to the decrease of soil strength and further caused the failure of the canal slope.

The soil samples were collected from the debris of the failed slope at a depth of approximately 1 m (i.e. within the frost and active zone depth) before the slope renovation. The natural moisture content (w_n) and dry density (ρ_{dn}) were measured during the sampling, which are 26.3% and 1540 kg/m^3, respectively. The basic index properties of this soil are summarized in Table 1.

X-ray fluorescence spectrometry (XRF) tests were performed to reveal the soil's dominant chemical components, which are SiO$_2$: 60.48%, Al$_2$O$_3$: 18.53%, Fe$_2$O$_3$: 6.63%, K$_2$O: 3.05%, and CaO: 4% (by dry mass). The soil's major mineral components determined by X-ray diffraction (XRD) tests are quartz, illite, albite, and calcite. The free swelling ratio (i.e. percentage of volumetric increment of dry and grounded soil powders when soaked in water) of the soil is 67%. According to the Chinese technical code for buildings in expansive soil regions GB 50,112–2013 (Ministry of Housing and Urban–Rural Development 2013), this soil is classified as an expansive soil with medium-swell potential. The soil has a plasticity index (I_P) of 21. According to the guideline of Peck et al. (1974) which is based on the I_P, this soil has medium to high swelling potential. Although from the mineralogical perspective (generally in agricultural and geological practice), the soil has a significant portion of silt and contains illite that is not as hydrophilic as the montmorillonite, the free swelling ratio, physical properties, and the associated form of slope failure all suggest that the soil demonstrates nonnegligible swelling potentials that pose threats to the geo-structures. Thus, from the geotechnical engineering perspective, the soil can be regarded as expansive soil.

Specimen preparation

The collected soil samples were air-dried, pulverized, and passed through a 2.0-mm-opening sieve to remove large particles. To simulate the field condition, the prepared dry soil was mixed with distilled water to reach the natural moisture content of 26.3%. The moist soil was statically compacted in three layers in a cylindrical stainless-steel mould with an inner diameter of 38 mm and a height of 76 mm.

Table 1 Basic index properties of the tested expansive soil

Properties	Values
Specific gravity, Gs	2.68
Liquid limit, wL (%)	42.84
Plastic limit, wP (%)	22.40
Plasticity index, IP	20.44
Shrinkage limit, wS (%)	8.50
Sand (%)	18
Silt (%)	70
Clay (%)	12
Free swelling ratio (%)	67
pH value	8.2
USCS	CL
AASHTO	A-7–6

The specimens were compacted to the natural dry density of 1540 kg/m³. Compacted specimens were immediately extracted from the mould, wrapped by plastic films, and placed in sealed plastic bottles for 72 h at room temperature of 25 ± 1 °C to achieve moisture equilibrium. Thereafter, some as-compacted specimens were directly used for microstructure investigations and triaxial tests (referred to as untreated specimens hereafter). Other specimens were exposed to DW, FT, or DWFT cycles before subjecting to these tests.

Application of DW, FT, and DWFT cycles

Relevant studies suggested that the mechanical behaviour and microstructure of clayey soils generally come into equilibrium after 5 to 7 cycles of DW and FT actions (Liu et al. 2016; Lu et al. 2019; Hu et al. 2019). Therefore, to reveal the evolution and final status of the soil's structure and mechanical properties, specimens in this study were subjected to 1, 4, 6, and 10 DW, FT, or DWFT cycles.

During DW cycles, the moisture content of specimens varied between the saturated water content (w_{sat}) and shrinkage limit (w_s). In one DW cycle, specimens were firstly dried from w_n to w_s and then wetted to w_{sat}. They were afterward dried to the w_n. During drying, specimens were entirely wrapped in filter papers and placed in a temperature and humidity control box where they were dried under a temperature of 25 °C and relative humidity (RH) of 60%. It was found that under an RH = 60%, the specimens dried slowly, and only very few desiccation cracks were found on the surface of the specimens. It typically took about 5 to 6 days to dry the specimens from w_{sat} to w_s. During wetting, specimens were entirely covered in filter papers and were periodically (every 24 h) sprayed with distilled water. After each spray, specimens along with the moist filter papers were wrapped in plastic film for moisture equilibrium of 24 h. This procedure was repeated until w_{sat} was achieved. After wetting, the specimens were cut into 10 to 15 small blocks to measure their moisture contents. The differences between the moisture content of soil blocks near the surface and the soil blocks at the core of the specimens were always within 0.2%, confirming that the moisture distribution was uniform within the specimens. Such slow drying and wetting processes help to reduce the nonuniform volumetric strain and the associated development of cracks (Han and Vanapalli 2016).

Closed-system FT cycles were utilized to apply FT histories to the specimens considering the low permeability of expansive soils (especially under unsaturated and frozen conditions) which does not allow significant water migration during freezing (Chamberlain 1973). Specimens wrapped in plastic film and sealed in bottles were directly placed in the temperature and humidity control box. In one FT cycle,

specimens were firstly frozen at −20 °C for 12 h and then allowed to thaw at 25 °C for 12 h. The temperature range during FT cycles was determined based on the local annual temperature range in Qiqihar (i.e. −18.6 to 23.1 °C).

In one DWFT cycle, specimens were firstly subjected to one DW cycle and then subjected to one FT cycle immediately afterward. This procedure repeats until the designated number of DWFT cycles was applied.

Measurement of volumetric change

To trace the volumetric behaviour during DW, FT, and DWFT cycles, volume measurements were conducted on specimens after each drying, wetting, freezing, and thawing process using an electronic Vernier calliper with an accuracy of 0.005 mm. Diameter (i.e. d_1, d_2, and d_3) and height (i.e. h_1, h_2, and h_3) measurements were taken at three respective cross-sections that are evenly distributed on the surface of the specimen. The measurements were taken very carefully and gently in order not to disturb the specimens, especially the weak and wet specimens after thawing. The average values of diameter and height measurements were used to calculate the volume of the specimens and further, the volumetric strain (ε_v) during DW, FT, and DWFT cycles.

MIP and SEM tests

MIP tests were conducted on untreated specimens and specimens subjected to 1, 4, and 10 FT, DW, and DWFT cycles. SEM tests were performed on untreated specimens and specimens subjected to 10 FT, DW, and DWFT cycles. Samples used for MIP and SEM tests were 1–2 g in weight and were sampled from compacted specimens following the procedures introduced by Lin and Cerato (2014). The freeze-drying method using nitrogen was employed to dehydrate the samples before the MIP and SEM tests. This method was considered capable of preserving the soil structure during drying (Delage and Lefebvre 1984; Penumadu and Dean 2000; Sasanian and Newson 2013). A PoreMaster 33 porosimeter was used to perform the MIP tests, and A FEI Quanta 200 machine was used for the SEM tests.

Triaxial consolidated undrained test

After the application of FT, DW, and DWFT cycles, specimens were vacuum saturated for 24 h. They were thereafter transferred to the triaxial cell where they were further back-pressure saturated. An initial cell pressure (σ_c) of 30 kPa and an initial back pressure (σ_b) of 20 kPa were applied. They were then increased simultaneously at an interval of 20 kPa until the pore-water pressure parameter; B exceeds 0.90 (Kamruzzaman et al. 2009). After back-pressure saturation, the consolidation stage followed

during which the σ_b kept constant, while the σ_c increases to consolidate the specimens at effective confining pressure σ'_c ($\sigma'_c = \sigma_c - \sigma_b$) levels of 50, 100, 200, and 300 kPa. The consolidation process was considered finished when the volume of discharged water approached constant and the excess pore water pressure had dissipated (Thu et al. 2006). Finally, the specimens were sheared under undrained conditions at an axial displacement rate of 0.066%/min until the axial strain reached 20%.

Test results and discussions

Volumetric behaviour

The volumetric strain (ε_v) of specimens during DW, FT, or DWFT cycles is defined by Eq. 1.

$$\varepsilon_v = (V_N - V_0)/V_0 \times 100\% \qquad (1)$$

where V_0 is the initial volume of the untreated specimen, V_N is the volume of the specimen after N cycles of DW, FT, or DWFT processes. Positive ε_v indicates swelling while negative ε_v refers to shrinkage.

The evolution of ε_v during DW, FT, and DWFT cycles is shown in Fig. 3 where letters D, W, F, and T indicate drying, wetting, freezing, and thawing processes, respectively. Eventually, DW cycles result in shrinkage ($\varepsilon_v = -3\%$ after 10 DW cycles), while FT cycles lead to slight swelling ($\varepsilon_v = 1.2\%$ after 10 FT cycles) in the specimens' volume. The scale of the variation in the ε_v during DW cycles is higher than that during FT cycles. The two opposite volumetric behaviours offset during DWFT cycles and result in shrinkage of the specimens ($\varepsilon_v = -2.2\%$ after 10 DWFT cycles). The ε_v during the initial several DW, FT, and DWFT cycles are significant, but its scale reduces with an increasing number of DW, FT, and DWFT cycles (hereafter denoted as N_{DW}, N_{FT}, and N_{DWFT}).

The volumetric behaviour becomes elastic after approximately 4 DW, FT, or DWFT cycles. In other words, the accumulation of non-recoverable ε_v becomes almost negligible when N_{DW}, N_{FT}, or N_{DWFT} exceed 4. These observations are consistent with similar studies (Viklander 1998; Tripathy et al. 2002; Wang and Wei 2014; Estabragh et al. 2015; Zeng et al. 2018) and indicate that specimens' microstructure has come into an equilibrium status (Sridharan and Allam 1982; Dif and Blumel 1991; Basma et al. 1996; Zhang et al. 2006).

Evolution of soils' microstructure

Based on the volumetric behaviours shown in Fig. 3, it is reasonable to assume that the soil's microstructure has reached equilibrium after 10 DW, FT, and DWFT cycles.
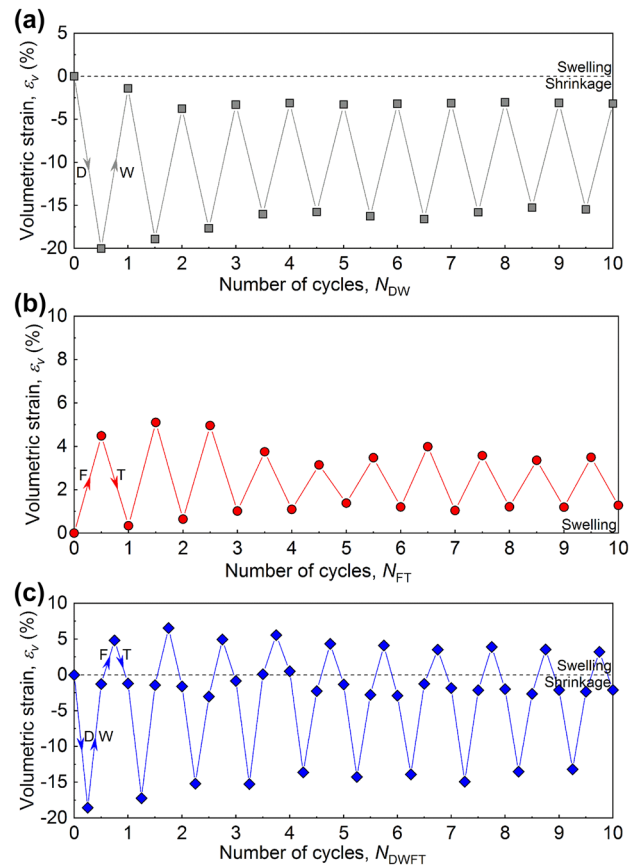

Fig. 3 Evolution of volumetric strains during the **a** DW, **b** FT, and **c** DWFT cycles

Figure 4 shows MIP results of untreated specimens and specimens subjected to 10 DW, FT, and DWFT cycles in the form of cumulative intrusion (CI) curves (Fig. 4a) and pore size distribution (PSD) curves (Fig. 4b). The CI curves are defined as the relationship between the void ratio intruded by mercury e_{MIP} ($e_{MIP} = V_m/V_s$ where V_m is the volume of intruded mercury and V_s is the volume of the soil solids) and the corresponding pore diameter d. The derivatives of CI curves (i.e. $-\delta e_{MIP}/\delta \log d$ versus $\log d$ relationships) are the PSD curves. The corresponding SEM images are shown in Fig. 5.

The PSD curve of the untreated specimen is bimodal with two peaks at about 1.3 µm and 30 µm, respectively. Such a bimodal PSD curve is typical for compacted soils (Burton et al. 2015). Macropores about 30 µm in dimension can be observed from the SEM image (Fig. 5a). To evaluate the influence of DW, FT, and DWFT cycles on the microstructure, the CI and PSD curves were divided into A, B, and C zones by two boundaries defined at 0.1 µm and 5 µm (see Fig. 4). A total of 0.1 µm is a demarcation value at the left side of which there is nearly no effect of cyclic treatments on PSD curves. Referencing
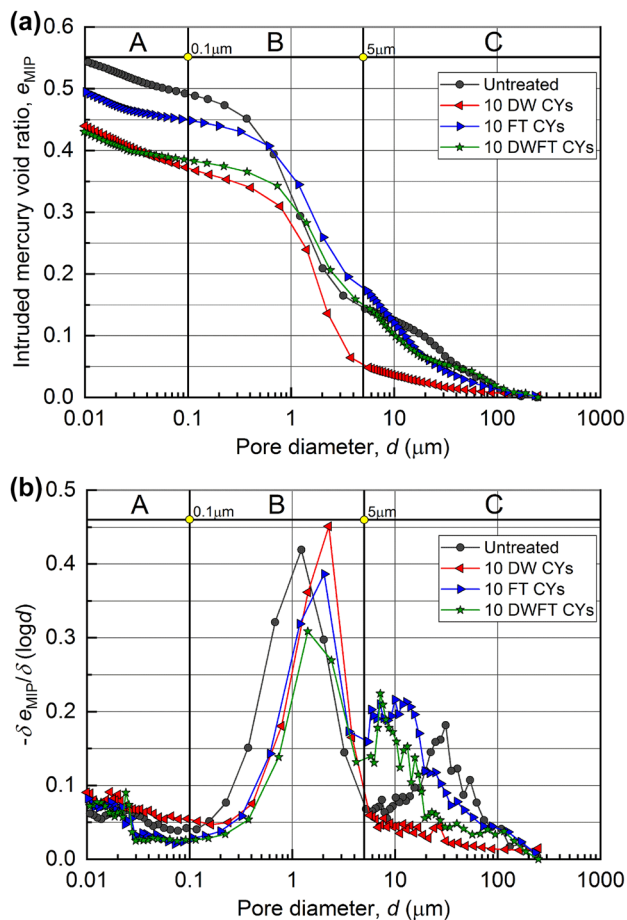
Fig. 4 The **a** cumulative intrusion (CI) curves and **b** pore size distribution (PSD) curves of specimens untreated and after 10 DW, FT, and DWFT cycles

the criterion suggested by Burton et al. (2015), 5 µm is the general turning point for all PSD curves and thus is used as the delimiting boundary which separates the macropores and micropores. Void ratio in the A, B, and C zones (denoted as $e_{MIP,A}$, $e_{MIP,B}$, $e_{MIP,C}$) can be computed from $e_{MIP,A} = e_{MIP,0.01} - e_{MIP,0.1}$, $e_{MIP,B} = e_{MIP,0.1} - e_{MIP,5}$, $e_{MIP,C} = e_{MIP,5}$ where $e_{MIP,N}$ is the e_{MIP} value at Nµm. Their values are summarized in Table 2.

The following can be observed in Fig. 5 and Table 2:

(i) In Zone A, DW, FT, and DWFT cycles impose trivial influence on the shape of the CI and PSD curves as well as the value of $e_{MIP,A}$.

(ii) In Zone B, the $e_{MIP,B}$ decreases during DW, FT, and DWFT cycles. The decrease is most significant during DWFT cycles but is slight during DW cycles. The peak of the micropores shifts to the right, indicating a slight increase in the diameter of the dominant micropores. The frequency (i.e. $-\delta e_{MIP}/\delta \log d$) corresponding to the peak, however, increases after

10 DW cycles but decreases after 10 FT or DWFT cycles.

(iii) In Zone C, the peak of macropores in the PSD curve completely disappears after 10 DW cycles, suggesting that the macropores are unstable upon moisture changes. This is accompanied by a significant decrease in the $e_{MIP,C}$. The collapse of the macropores is also reflected in the SEM image in Fig. 5c where the soil structure becomes uniform and the compaction-induced macropores (see in Fig. 5a) are erased.

(iv) In Zone C, dominant macropores with diameters of 30 µm also collapse but FT-induced cracks emerge and develop after 10 FT cycles (see Fig. 5b). The dimension of these cracks is random and varies between 5 and 20 µm, constituting a plateau in the PSD curve. Similar behaviours are also observed for specimens subjected to 10 DWFT cycles. However, due to the offset between the effects of FT cycles and DW cycles, the dimension and amount of the induced cracks are smaller than the FT-induced cracks (compare cracks in Fig. 5b and d) and concentrates at about 7 µm.

It should be noted that the total intruded void ratio (i.e. $e_{MIP0.01}$) of the specimen after 10 FT cycles is lower than that of the untreated specimen (see Fig. 4a), while the volumetric expansion was observed from FT specimens (see Fig. 3b). This is due to the existence of FT-induced cracks with dimensions that are larger than the maximum pore diameter a MIP test can detect (about 250 µm). These cracks are visible to naked eyes, but their volume is not reflected by the CI curves.

The volumetric behaviour of the soil is closely related to the evolution of its microstructure. During DW cycles, the collapse of the macropores and the remarkable reduction in the $e_{MIP,C}$ lead to the final shrinkage of the global volume. On the other hand, the development of the cracks during FT cycles creates extra pore space and increases the $e_{MIP,C}$ as well as in global volume. The collapse of the macropores and development of cracks offset during DWFT cycles and lead to an intermediate volumetric behaviour.

Figure 3 shows that the scale of the ε_v decreases with increasing N_{DW}, N_{FT}, or N_{DWFT} in the first few cycles before reaching equilibrium. This is generally due to two reasons: (i) the initial ε_v contains plastic and elastic strain, while the plastic strain quickly decreases during the first few cycles and (ii) cracks induced by DW and FT cycles reduce the integrity of the soil structure and segregate the soil matrix. The deformation during DW and FT cycles was partly offset by the widening of these cracks.

Fig. 5 SEM images of **a** untreated specimens and specimens after **b** 10 FT cycles, **c** 10 DW cycles, and **d** 10 DWFT cycles
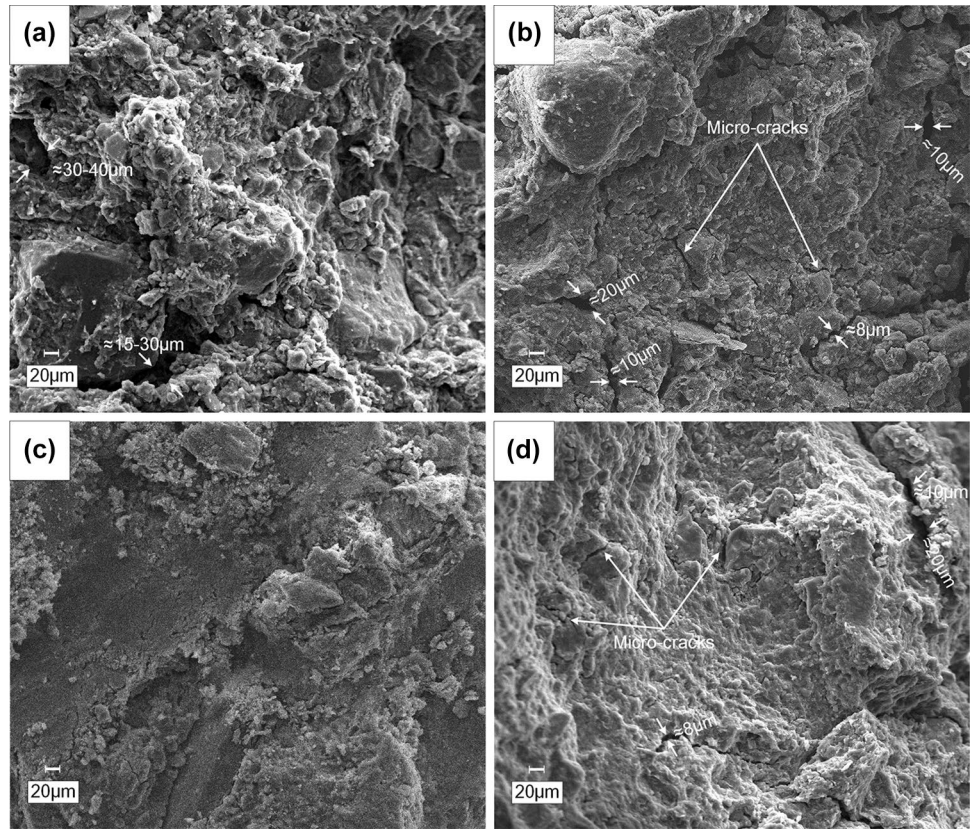
Shear strength and elastic modulus during consolidated undrained shearing

Figures 6, 7, and 8 summarize the stress–strain relationships (i.e. deviator stress q versus axial strain ε_1; $q = \sigma_1 - \sigma_3$, σ_1 is the major principal stress and σ_3 is the minor principal stress, $\sigma_3 = \sigma_c$) during consolidated undrained shearing for specimens subjected to DW, FT, and DWFT cycles. Seating errors were corrected in these relationships following the approach suggested by Atkinson and Evans (1985). It can

Table 2 Evolution of the eMIP after 1, 4, 10 FT, DW, and DWFT cycles

Cycle types	ΔeMIP,A	ΔeMIP,B	ΔeMIP,C
Untreated	0.062	0.345	0.146
1 DW cycles	0.067	0.300	0.082
4 DW cycles	0.075	0.296	0.091
10 DW cycles	0.083	0.317	0.055
1 FT cycles	0.059	0.336	0.123
4 FT cycles	0.056	0.293	0.183
10 FT cycles	0.059	0.272	0.177
1 DWFT cycles	0.078	0.317	0.124
4 DWFT cycles	0.065	0.279	0.132
10 DWFT cycle	0.054	0.233	0.152

be observed that the stress–strain curves of all specimens (regardless of the type and number of treatments) belong to the strain-stabilization type under low σ_c (i.e. 50, 100 kPa). For higher σ_c (i.e. 200, 300 kPa), the stress–strain curves start to show strain-hardening characteristics.

To determine the soil's undrained elastic modulus and shear strength, the stress–strain curves were fitted using the hyperbolic model (Eq. 1) proposed by Kondner (1963).

$$q = \frac{\varepsilon_1}{a + b\varepsilon_1} \tag{2}$$

where a and b are model parameters. According to Gutierrez et al. (2008), Moniz (2009), and Ladd et al. (1977), $1/a$ is the slope of the initial curve and equals the undrained elastic modulus, E_u. $1/b$ is the ultimate deviator stress and indicates the undrained shear strength, q_u.

Mohr–Coulomb model (Eq. 3) was used to interpret the undrained shear test results and determine the soil's cohesion (c, kPa) and internal friction angle (ϕ, °) in terms of total stress.

$$\sigma_1 = \frac{2c\cos\phi}{1 - \sin\phi} + \frac{1 + \sin\phi}{1 - \sin\phi}\sigma_3 \tag{3}$$

Variation of the determined q_u, E_u, c, and ϕ with N is summarized in Figs. 9, 10, and 11, respectively. A power
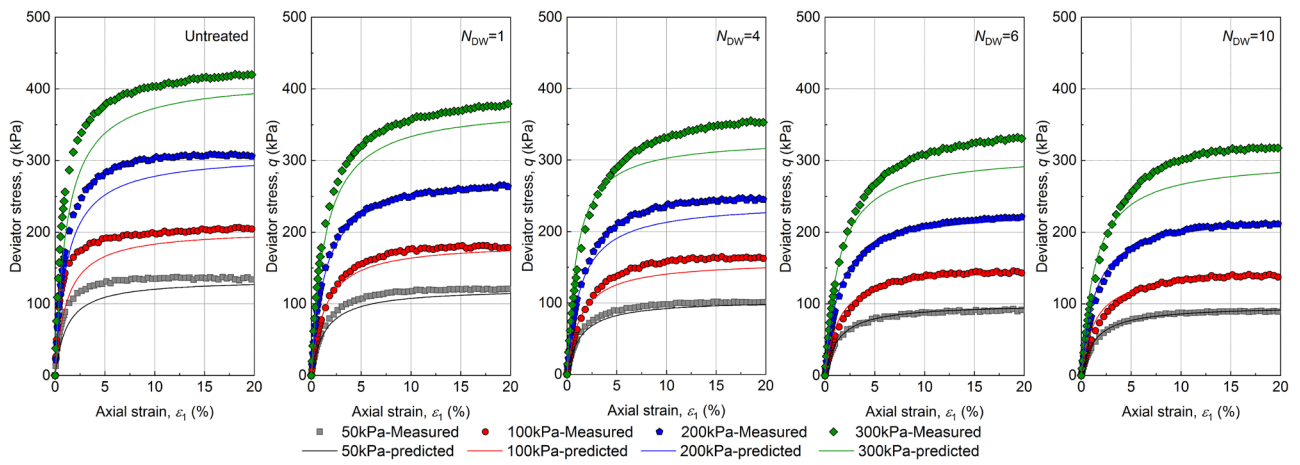
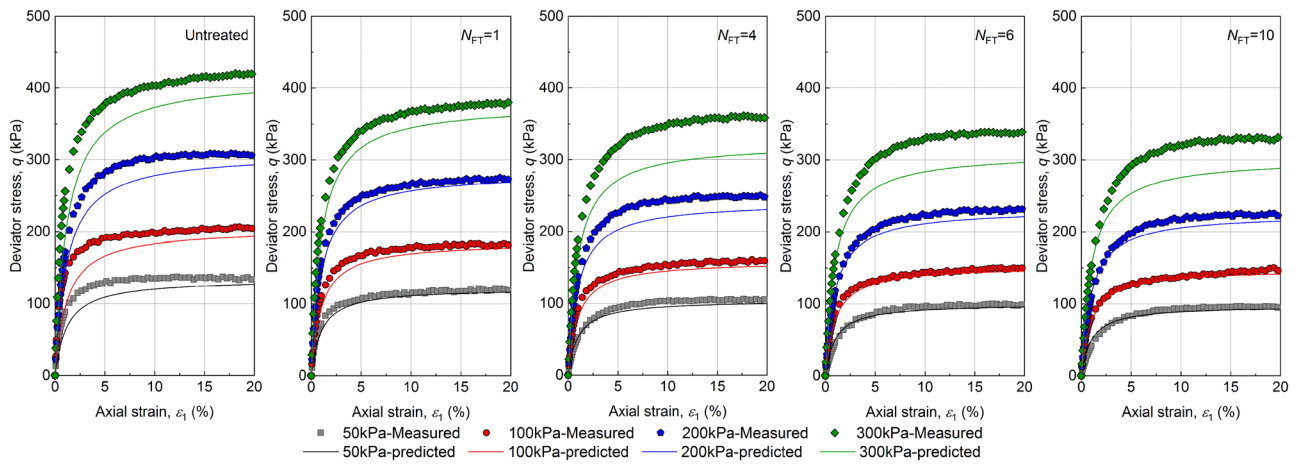**Fig. 6** Stress–strain relationships after DW cycles

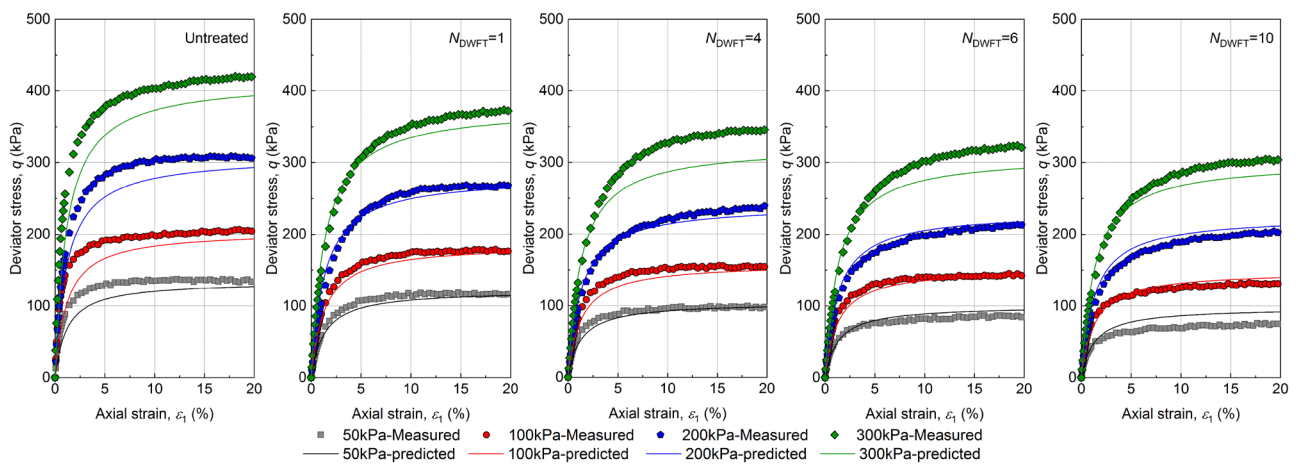**Fig. 7** Stress–strain relationships after FT cycles
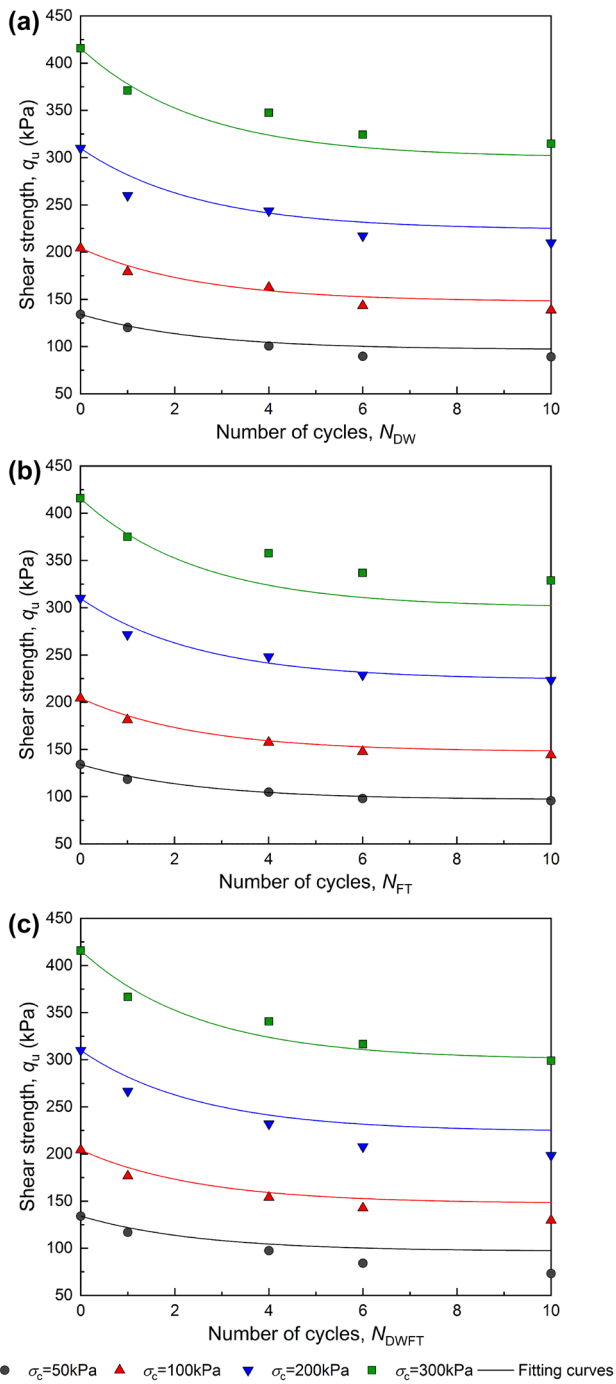

Fig. 8 Stress–strain relationships after DWFT cycles

Fig. 9 Variation of shear strengths after **a** DW, **b** FT, and **c** DWFT cyclic treatments

Fig. 10 Variation of elastic modulus of specimens after **a** DW, **b** FT, and **c** DWFT cyclic treatments

function (Eq. 4) is adopted to describe the reduction of q_u, E_u, c, and ϕ with N.

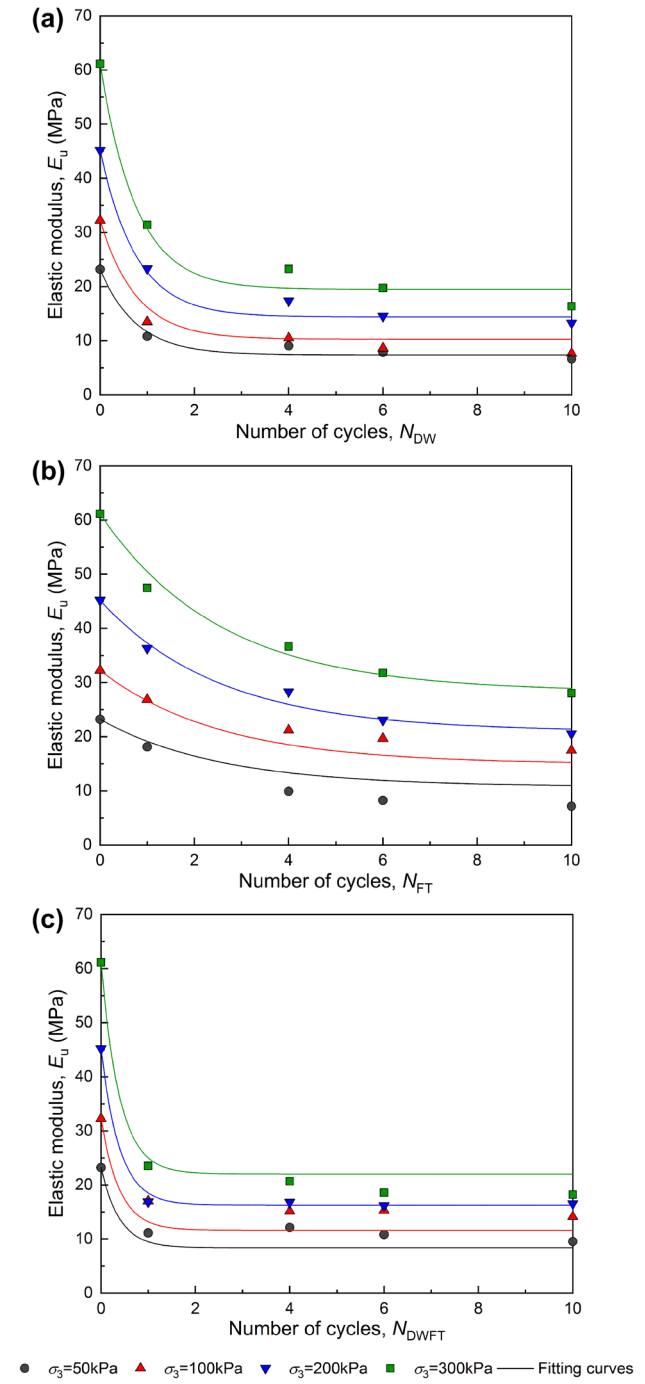$$\frac{\Omega_N}{\Omega_0} = \frac{1 + \alpha e^{-\beta N}}{1 + \alpha} \qquad (4)$$

where Ω_0 collectively represents the q_u, E_u c, or ϕ of untreated specimens; Ω_N is the q_u, E_u c, or ϕ after N cycles of treatment; α and β are model parameters; and e is the base of the natural logarithm and equals 2.7182. The fitting curves are shown in Figs. 9, 10, and 11, and the fitting parameters (i.e. α, and β) are summarized in Table 3. The following can be observed:
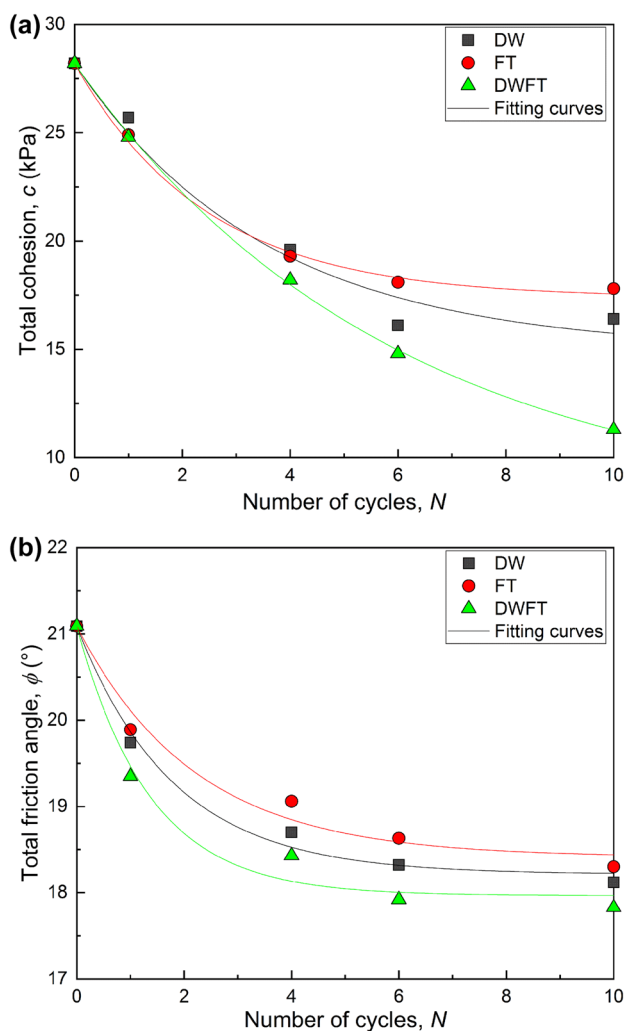
Fig. 11 Evolution of (**a**) total cohesion and (**b**) total friction angle with the increase of cycle numbers

(i) The E_u, c, and ϕ decrease with DW, FT, and DWFT cycles, and their behaviours are consistent. The decrease is comparatively more significant during DW cycles than FT cycles. The most remarkable reduction takes place during DWFT cycles due to the combined damages of FT and DW cycles. They reach an equilibrium after approximately 6 cycles. These observations are consistent with similar studies in the

literature (Rosa et al. 2017; Zeng et al. 2018; Wang et al. 2019; Tian et al. 2019; Tang et al. 2018; Han et al. 2018; Hossain et al. 2016).

(ii) The σ_c appears to have less impact on the E_u-N relationships, and the same pair of α and β values can suitably describe the E_u-N relationships under different σ_c.

(iii) For q_u specifically, the DW, FT, and DWFT cycles have similar effects on the q_u-N relationships because a unique pair of α and β values well describes the q_u-N relationships under all types of treatment under different σ_c.

Modelling stress–strain behaviours

A simple normalized model is developed to describe all stress–strain curves of the tested specimens after different DW, FT, and DWFT cycles, as shown in Figs. 6, 7, and 8. Reordering Eq. 2, substituting $1/a = E_u$ and $1/b = q_u$, and multiplying both sides by a normalization factor X yield (Eq. 5).

$$X\frac{\varepsilon_1}{q} = \frac{X}{E_u} + \frac{X}{q_u}\varepsilon_1 \qquad (5)$$

To normalize Eq. 5, factors X/E_u and X/q_u must be constants such that the right side of Eq. 5 is independent of σ_c. The σ_c, q_u, and E_u are typical candidates for factor X when normalizing stress–strain curves (Xu et al. 2005). q_u is adopted in this study as the X due to two reasons: (i) q_u is one of the simplest and most widely used soil properties in geotechnical practice and (ii) the q_u-N relationships during DW, FT, and DWFT cycles are similar and can be described by a unique equation. Substituting $X = q_u$ into Eq. 5 yields Eq. 6.

$$q_u\frac{\varepsilon_1}{q} = \frac{q_u}{E_u} + \varepsilon_1 \qquad (6)$$

The E_u-q_u relationships for each type of treatment are consistent regardless of the differences in the σ_c and the number of treatments, as shown in Fig. 12. They can be well fitted by linear equations, which show that q_u/E_u equals

Table 3 Values of parameters in Eq. 4

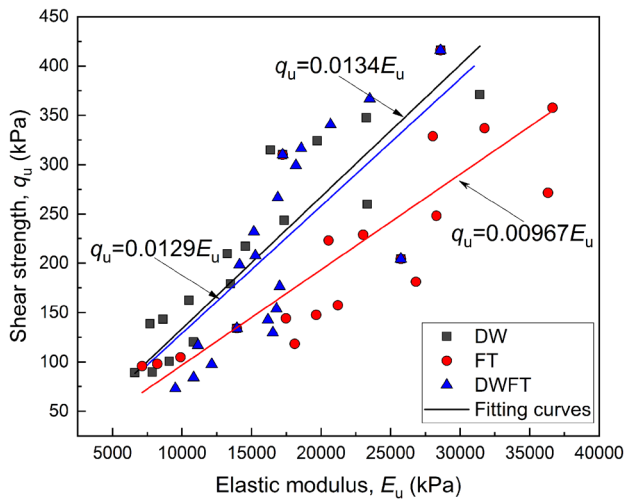| Parameter types	DW cycles		FT cycles		DWFT cycles	
	α	β	α	β	α	β
qu	0.386	0.395	0.386	0.395	0.386	0.395
Eu	2.141	1.314	1.161	0.393	1.777	2.566
c	0.888	0.281	0.623	0.408	2.769	0.170
ϕ	0.158	0.555	0.145	0.454	0.174	0.733

Fig. 12 Relationship of the elastic modulus and shear strength for specimens of DWFT cycle

0.00967 for FT cycles, 0.0134 for DW cycles, and 0.0129 for DWFT cycles.

Based on Eq. 4, the q_u-N relationship can be expressed as Eq. 7.

$$q_{uN} = q_{u0} \left(\frac{1 + \alpha e^{-\beta N}}{1 + \alpha} \right) \tag{7}$$

where q_{uN} and q_{u0} are the q_u of specimens after N cycles of DW, FT, or DWFT treatment and before treatment, respectively. Substituting Eq. 7 into Eq. 6 yields the normalized expression of q-ε_1 relationship.

$$q = q_{u0} \left(\frac{1 + \alpha e^{-\beta N}}{1 + \alpha} \right) \frac{\varepsilon_1}{\varepsilon_1 + \frac{q_u}{E_u}} \tag{8}$$

It is noted that α and β are constants regardless of σ_c and the number and type of treatments ($\alpha = 0.398$, $\beta = 0.395$; see Table 3). The stress–strain curves predicted by Eq. 8 are shown in Figs. 6, 7, and 8. It can be observed that good agreements are achieved between the measurements and the predictions of Eq. 8.

Conclusions

In this paper, the influence of multiple DW, FT, and DWFT cycles on the microstructure and mechanical behaviours (including volumetric behaviour, stress–strain behaviour during consolidated undrained shearing, undrained shear strength parameters, and undrained elastic modulus) of an expansive soil was investigated. The following observations and conclusions were obtained from the experimental studies:

(i) Compaction-induced macropores in the range of 5 to 250 μm collapse during DW cycles. In the same dimension range, FT cycles introduce cracks into the soil structure. These two types of opposite influences offset during the DWFT cycles and result in an intermediate soil structure. DW, FT, and DWFT cycles appear to have a minor influence on the micropores with diameters less than 5 μm.

(ii) The tested soil swelled during FT cycles but shrank during DW cycles. The interplay of the two opposite volumetric behaviours results in slight shrinkage of the soil during DWFT cycles. The volumetric behaviours become elastic after approximately 4 cycles during all three types of treatments.

(iii) The q_u, E_u, c, and ϕ reduce during DW, FT, and DWFT cycles, and the reduction is most significant during DWFT cycles due to the combined damage of FT and DW processes. The reduction comes to equilibrium after approximately 6 cycles.

A simple normalized model is developed to predict the stress–strain curves of specimens undergoing 0, 1, 4, 6, and 10 DW, FT, and DWFT cycles. The performance of this model is verified by the triaxial compression test results. The model presented in this paper could be useful for the estimation of the mechanical behaviours of expansive soils in seasonally frozen regions.

Declarations

Conflict of interest The authors declare no competing interests.

References

Ajdari M, Habibagahi G, Masrouri F (2013) The role of suction and degree of saturation on the hydro-mechanical response of a dual porosity silt-bentonite mixture. Appl Clay Sci 83:83–90

Albrecht BA, Benson CH (2001) Effect of desiccation on compacted natural clays. J Geotech Geoenviron 127:67–75

Aldaood A, Bouasker M, Al-Mukhtar M (2014) Impact of wetting-drying cycles on the microstructure and mechanical properties of lime-stabilized gypseous soils. Eng Geol 174:11–21

Al-Homoud AS, Basma AA, Husein Malkawi AI, Al-Bashabsheh MA (1995) Cyclic swelling behaviour of clays. J Geotech Eng 121(7):562–565

Alonso EE, Gens A, Hight DW (1987) Special problems soils General Rep. In: European Conference on Soil Mechanics and Foundation Engineering, Dublin, Ireland

Alonso EE, Romero E, Hoffmann C, García-Escudero E (2005) Expansive bentonite–sand mixtures in cyclic controlled-suction drying and wetting. Eng Geol 81(3):213–226

Atkinson JH, Evans JS (1985) Discussion on: The measurement of soil stiffness in the triaxial apparatus by RJ Jardine MJ Symes and JB Burland. Geotechnique 35(3):378–382

Aubert JE, Gasc-Barbier M (2012) Hardening of clayey soil blocks during freezing and thawing cycles. Appl Clay Sci 65:1–5

Basma AA, Al-Homoud AS, Malkavi AIH, Al-Bashabshah MA (1996) Swelling-shrinkage behaviour of natural expansive clays. Appl Clay Sci 11:211–227

Burton GJ, Pineda JA, Sheng D, Airey D (2015) Microstructural changes of an undisturbed reconstituted and compacted high plasticity clay subjected to wetting and drying. Eng Geol 193:363–373

Chamberlain EJ (1973) A model for predicting the influence of closed-system freeze-thaw on the strength of thawed soil. Symposium on Frost Action Roads, Oslo, pp 94–97

Cui ZD, He PP, Yang WH (2014) Mechanical properties of a silty clay subjected to freezing-thawing. Cold Reg Sci Technol 98:26–34

Dalla Santa G, Cola S, Secco M, Tateo F, Sassi R, Galgaro A (2019) Multiscale analysis of freeze–thaw effects induced by ground heat exchangers on permeability of silty clays. Géotechnique 69(2):95–105

Delage P, Lefebvre G (1984) Effect of air drying and critical point drying on the porosity of clay soils. Can Geotech J 21:181–185

Dif AE, Blumel WF (1991) Expansive soils under cyclic drying and wetting. Geotech Test J 14(1):96–102

Edwin JC, Anthony JG (1979) Effect of freezing and thawing on the permeability and structure of soils. Eng Geol 13:73–92

Estabragh AR, Parsaei B, Javadi AA (2015) Laboratory investigation of the effect of cyclic wetting and drying on the behaviour of an expansive soil. Soils Found 55:304–314

Graham J, Au VCS (1985) Effects of freeze-thaw and softening on a natural clay at low stresses. Can Geotech J 22(1):69–78

Gutierrez M, Nygard R, Hoeg K et al (2008) Normalized undrained shear strength of clay shales. Eng Geol 99(1–2):31–39

Han Z, Vanapalli SK (2016) Stiffness and shear strength of unsaturated soils in relation to soil-water characteristic curve. Geotechnique 66(8):627–647

Han Y, Wang Q, Wang N, Wang J, Zhang X, Cheng S, Kong Y (2018) Effect of freeze-thaw cycles on shear strength of saline soil. Cold Reg Sci Technol 154:42–53

Hewitt RD, Daniel DE (1997) Hydraulic conductivity of geosynthetic clay liners after freeze-thaw. J Geotech Geoenviron Eng 123(4):305–313

Hohmann-Porebska M (2002) Microfabric effects in frozen clays in relation to geotechnical parameters. Appl Clay Sci 21(1–2):77–87

Hossain S, Kong LW, Song Y (2016) Effect of drying-wetting cycles on saturated shear strength of undisturbed residual soils. Am J Civ Eng 4(4):159–166

Hu C, Yuan Y, Mei Y et al (2019) Comprehensive strength deterioration model of compacted loess exposed to drying-wetting cycles. Bull Eng Geol Environ 79:383–398

Jones DE, Holtz WG (1973) Expansive soils - the hidden disaster. Civ Eng 43(8):49–51

Kalkan E (2011) Impact of wetting-drying cycles on swelling behavior of clayey soils modified by silica fume. Appl Clay Sci 52(4):345–352

Kamruzzaman AH, Chew SH, Lee FH (2009) Structuration and destructuration behavior of cement-treated Singapore marine clay. J Geotech Geoenviron Eng 135(4):573–589

Konrad JM, Samson M (2000) Hydraulic conductivity of kaolinite-silt mixtures subjected to closed-system freezing and thaw consolidation. Can Geotech J 37(4):857–869

Kondner RL (1963) Hyperbolic stress±strain response: cohesive soils. J. Soil Mech. and Foundation Engng Div. ASCE 89(1):115–143

Kraus JF, Benson CH, Erickson AE, Chamberlain EJ (1997) Freeze–thaw cycling and hydraulic conductivity of bento- nitic barriers. J Geotech Geoenviron Eng 123(3):229–238

Ladd CC, Foott R, Ishihara K (1977) Stress-deformation and strength characteristics state of the art. Rep Anon Proc 9th ICSMFE 2:421–440

Lin B, Cerato AB (2014) Applications of SEM and ESEM in microstructural investigation of shale-weathered expansive soils along swelling-shrinkage cycles. Eng Geol 177:66–74

Liu JK, Chang D, Yu QM (2016) Influence of freeze-thaw cycles on mechanical properties of a silty sand. Eng Geol 210:23–32

Lu N, Godt JW (2012) Hillslope hydrology and stability. University Press, Cambridge

Lu Y, Liu SH, Alonso E, Wang LJ, Xu L, Li Z (2019) Volume changes and mechanical degradation of a compacted expansive soil under freeze-thaw cycles. Cold Reg Sci Technol 157:206–214

Luo J, Tang L, Ling X, Geng L (2018) Experimental and analytical investigation on frost heave characteristics of an unsaturated moderately expansive clay. Cold Reg Sci Technol 155:343–353

Malusis MA, Yeom S, Evans JC (2011) Hydraulic conductivity of model soil-bentonite backfills subjected to wet-dry cycling. Can Geotech J 48(8):1198–1211

Massat L, Cuisinier O, Bihannic I, Claret F, Pelletier M, Masrouri F, Gaboreau S (2016) Swelling pressure development and inter-aggregate porosity evolution upon hydration of a compacted swelling clay. Appl Clay Sci 124:197–210

Ministry of Housing and Urban Rural Development PR, China (2013) Technical code for building in expansive soil regions (GB 50112–2013). China Construction Industry Press, Beijing (in Chinese)

Moniz SR (2009) The influence of effective consolidation stress on the normalized extension strength properties of resedimented Boston Blue Clay. Massachusetts Institute of Technology, Cambridge

Monroy R, Zdravkovic L, Ridley A (2010) Evolution of microstructure in compacted London Clay during wetting and loading. Geotechnique 60(2):105–119

Nowamooz H, Masrouri F (2008) Hydromechanical behaviour of an expansive bentonite/silt mixture in cyclic suction-controlled drying and wetting tests. Eng Geol 101(3–4):154–164

Othman M, Benson C (1993) Effect of freeze–thaw on the hydraulic conductivity and morphology of compacted clay. Can Geotech J 30(2):236–246

Peck RB, Hanson WE, Thornburn TH (1974) Foundation engineering, 2nd edn. John Wiley and Sons, New York

Peng X, Horn R, Smucker A (2007) Pore shrinkage dependency of inorganic and organic soils on wetting and drying cycles. Soil Sci Soc Am J 71(4):1095–1104

Penumadu D, Dean J (2000) Compressibility effect in evalu- ating the pore-size distribution of kaolin clay using mercury in- trusion porosimetry. Can Geotech J 37(2):393–405

Pires LF, Cooper M, Cássaro FAM, Reichardt K, Bacchi OOS, Dias NMP (2008) Micromorphological analysis to characterize structure modifications of soil samples submitted to wetting and drying cycles. CATENA 72:297–304

Qu YL, Ni WK, Niu FJ et al (2020) Mechanical and electrical properties of coarse-grained soil affected by cyclic freeze-thaw in high cold regions. J Cent South Univ 27:853–866

Rosa MG, Cetin B, Edil TB, Benson CH (2017) Freeze-thaw performance of fly ash-stabilized materials and recycled pavement materials. J Mater Civil Eng 29(6):04017015

Sasanian S, Newson TA (2013) Use of mercury intrusion porosimetry for microstructural investigation of reconstituted clays at high water contents. Eng Geol 158:15–22

Seiphoori A, Ferrari A, Laloui L (2014) Water retention behaviour and microstructural evolution of MX-80 bentonite during wetting and drying cycles. Geotechnique 64(9):721–734

Sridharan A, Allam MM (1982) Volume change behaviour of desiccated soil. J Geotech Eng 108:1057–1071

Tang CS, Wang DY, Shi B, Li J (2016) Effect of wetting-drying cycles on profile mechanical behavior of soils with different initial conditions. CATENA 139:105–116

Tang L, Cong S, Geng L, Ling X, Gan F (2018) The effect of freeze-thaw cycling on the mechanical properties of expansive soils. Cold Reg Sci Technol 145:197–207

Tang YQ, Yan JJ (2015) Effect of freeze-thaw on hydraulic conductivity and microstructure of soft soil in Shanghai area. Environ Earth Sci 73(11):7679–7690

Thu TM, Rahardjo H, Leong EC (2006) Shear strength and pore-water pressure characteristics during constant water content triaxial tests. Journal of Geotechnical and Geoenvironmental Engineering 132(3):411–419

Tian H, Wei C, Tan L (2019) Effect of freezing-thawing cycles on the microstructure of soils: A two-dimensional NMR relaxation analysis. Cold Reg Sci Technol 158:106–116

Tripathy S, Subba Rao KS, Fredlund DG (2002) Water content–void ratio swell-shrink paths of compacted expansive clays. Can Geotech J 39(4):938–959

Tripathy S, Kanakapura S, Rao S (2009) Cyclic swell–shrink behavior of a compacted expansive soil. Geotech Geol Eng 27:89–103

Viklander P (1998) Permeability and volume changes in till due to cyclic freeze-thaw. Can Geotech J 35(3):471–477

Vilar OM, Rodrigues RA (2011) Collapse behavior of soil in a Brazilian region affected by a rising water table. Can Geotech J 48(2):226–233

Wang G, Wei X (2014) Modeling swelling-shrinkage behavior of compacted expansive soils during wetting-drying cycles. Can. Geotech. J 52(6):783–794

Wang TL, Liu YJ, Yan H, Xu L (2015) An experimental study on the mechanical properties of silty soils under repeated freeze–thaw cycles. Cold Reg Sci Technol 112:51–65

Wang S, Ding J, Xu J, Ren J, Yang Y (2019) Shear Strength Behavior of Coarse- Grained Saline Soils after Freeze-Thaw. KSCE J Civ Eng 23(6):2437–2452

Wang S, Yang Z, Yang P (2017) Structural change and volumetric shrinkage of clay due to freeze-thaw by 3D X-ray computed tomography. Cold Reg Sci Technol 138:108–116

Xu J, Ren J, Wang Z, Wang S, Yuan J (2018) Strength behaviors and meso-structural characters of loess after freeze-thaw. Cold Reg Sci Technol 148:104–120

Xu S, Xu G, Cheng Y (2005) Normalization character of stress strain relations for clays. Geol Sci Technol Inf 42(s1):170–172 (in Chinese)

Xue Q, Wan Y, Chen Y et al (2014) Experimental research on the evolution laws of soil fabric of compacted clay liner in a landfill final cover under the dry-wet cycle. Bull Eng Geol Environ 73:517–529

Ye W, Li C (2019) The consequences of changes in the structure of loess as a result of cyclic freezing and thawing. Bull Eng Geol Environ 78(3):2125–2138

Yuen K, Graham J, Janzen P (1998) Weathering-induced fissuring and hydraulic conductivity in a natural plastic clay. Can Geotech J 35(6):1101–1108

Zeng Z, Kong L, Wang M, Sayem HM (2018) Assessment of engineering behaviour of an intensely weathered swelling mudstone under full range of seasonal variation and the relationships among measured parameters. Can Geotech J 55(12):1837–1849

Zha FS, Liu JJ, Xu L et al (2013) Effect of cyclic drying and wetting on engineering properties of heavy metal contaminated soils solidified/stabilized with fly ash. J Cent South Univ 20:1947–1952

Zhang R, Yang H, Zheng J (2006) The effect of vertical pressure on the deformation and strength of expansive soil during cyclic wetting and drying. In: Proceedings of the 4th International Conference on Unsaturated Soil, Arizona, USA, pp 894–905

Zhang F, Jing R, Feng D, Lin B (2015) Mechanical properties and an empirical model of compacted silty clay subjected to freeze-thaw cycles. In: International Symposium on Systematic Approaches to Environmental Sustainability in Transportation, Fairbanks City, p 200–212

Zhang Z, Ma W, Feng WJ, Xiao DH, Hou X (2016) Reconstruction of soil particle composition during freeze-thaw cycling: a review. Pedosphere 26(2):167–179

Zhao NF, Ye WM, Chen YG, Chen B, Cui YJ (2019) Investigation on swelling-shrinkage behavior of unsaturated compacted GMZ bentonite on wetting-drying cycles. Bull Eng Geol Environ 78(1):617–627

Zhou Z, Liu ZZ, Yang H et al (2020) Freeze-thaw damage mechanism of elastic modulus of soil-rock mixtures at different confining pressures. J Cent South Univ 27:554–565

Zou W, Han Z, Vanapalli SK, Zhang J, Zhao G (2018) Predicting volumetric behavior of compacted clays during compression. Appl Clay Sci 156:116–125